Chapter 1

Tomographic estimation of elliptical velocities

To estimate elastic constants from traveltime measurements it is first necessary to fit the traveltimes with elliptical velocity functions. As described in chapter 2, when the model is homogeneous and the axis of symmetry is vertical, only two parameters for each wave type are needed to describe the elliptical velocity functions. When the model is heterogeneous, however, the elliptical velocity functions need to be estimated at each point in space. Thus the problem of estimating them, which in homogeneous media is highly overdetermined, becomes in heterogeneous media a highly underdetermined problem. This chapter describes a tomographic approach for solving it. The underdeterminedness is resolved by using models for the heterogeneities that contain information about the expected variations in the medium. I show synthetic and field data examples that illustrate the application of the technique, which uses the anisotropic ray tracing algorithm developed in chapter 3.

1.1 Introduction

Depending on the degree of anisotropy and fine layering of the medium, tomograms obtained from cross-well traveltime data under an isotropic assumption may be significantly in error. These errors are analogous to the mispositions obtained with surface seismic methods when, in an anisotropic environment, stacking velocities are used to convert times into depths. The need to eliminate these errors provides one reason for using an anisotropic model in tomographic traveltime inversion. Another reason is that we are solving more than an imaging problem, since it is well known that anisotropy is a useful tool for studying lithology and the degree of stratification in sedimentary rocks. Taking velocity anisotropy into account in tomographic traveltime inversion helps us to gain useful information about reservoir and nonreservoir rocks.

Additional subsurface information (e.g., layer depths or vertical slownesses) is required for estimating anisotropy from surface seismic measurements (Levin, 1978). For this reason, in recent studies where anisotropy has been quantified, either a dif-

ferent geometry like VSP has been used (Byun and Corrigan, 1990; White et al., 1983) or the surface seismic information has been combined with well-logs (Banik, 1984). Observing that velocity anisotropy does not affect *P*-wave horizontal moveout considerably, Winterstein (1986) estimated the required layer thicknesses using velocities obtained form *P*-wave velocity analysis. Then, from *SH*-wave velocity analysis, he was able to estimate velocity anisotropy.

The main difference between tomographic velocity estimation from surface measurements and cross-well or VSP traveltimes is that the former requires a priori knowledge of reflector positions whereas the other methods do not. The only positions needed to estimate velocities from direct path, cross-well traveltimes are the source and receiver locations. Eliminating reflector mapping from the problem may make the estimation of other effects such as velocity anisotropy simpler in the cross-well environment. However, fewer attempts have been made to estimate velocity anisotropy from cross-well measurements. Stewart (1988) and Williamson et al. (1993) has proposed a modification to methods based on algebraic reconstruction techniques to include the effect of anisotropy. By using the weak anisotropy expression for the phase velocities given by Thomsen (1986) to fit the traveltimes, Stewart and Williamson et al. appear to assume the equality of group and phase velocities, which is, in general, not true. McCann et al. (1989) show how an isotropic inversion improved after assuming a fixed amount of anisotropy. Winterstein and Paulsson (1990) have estimated a vertical velocity gradient from VSP and cross-well data assuming a transversely isotropic model. Chapman and Pratt (1992) and Pratt and Chapman (1992) estimated velocity anisotropy in a general 2-D medium assuming weak anisotropy in order to justify isotropic ray tracing. Saito (1991) and Lines (1992) proposed to separate the effects of anisotropy and heterogeneity by first "removing" the anisotropy effects from the data so that conventional isotropic tomography in heterogeneous media can later be applied.

As I show in chapter 2, a general TI medium can be approximated by fitting *P*- and *S*-wave traveltimes with ellipses either around the horizontal or around the vertical (assuming a vertical axis of symmetry). Muir (1990), and Dellinger et al. (1993) show that when *P*- and *S*-wave traveltimes around both the horizontal and the vertical are available, a general TI medium can also be approximated by fitting the data with ellipses. What is needed to use these two different approximations in heterogeneous media is a procedure to find the parameters that describe the ellipses as a function of the position. This chapter focuses on such a procedure.

I show in this chapter how to fit tomographically transmitted traveltimes with heterogeneous elliptically anisotropic models. When *P*- and *S*-wave traveltimes are available, the images obtained can be transformed into elastic constants of a TI media as explained in chapter 2. I also show that if only one wave type is available, the images obtained can still provide useful information about the medium. The model of heterogeneities is required to be piecewise continuous and the formulation is identical for any wave type. No assumptions are made about the weakness of either anisotropy or heteroneneities.

Certain types of azimuthally anisotropic media can approximated with the model of velocity and heterogeneity used in this chapter, in particular those formed by dipping transversely isotropic layers. This is done by also considering as a variable the inclination of the axis of symmetry. The estimation of this variable may help the interpreter to characterize the amount of structural deformation that has undergone the different formations in the reservoir and may also help in the identification of structural unconformities.

I have studied the effects of the limited view of the measurements (from cross-well geometries) in the estimation of both slowness components for different models of heterogeneity, concluding that the technique is stable and accurate when used to invert 1-D (layered) models if the range of ray angles is "wide enough." In 2-D models, the estimation of lateral variations in the vertical component of the slowness is particularly difficult from cross-well geometries alone. Consequently, 2-D spatial variations in velocity anisotropy cannot be estimated at the same resolution as that of variations in velocity. I also show that when iterative techniques such as conjugate gradients are used to estimate the anisotropic parameters, early termination of the iterations (a way to damp the solution) may produce artificial anisotropy. This problem worsens in two dimensions.

A theoretical discussion of the technique is followed by examples with cross-well synthetic data and field data from an Amoco Gulf Coast site and the British Petroleum (BP) Devine test site.

1.2 Forward modeling

The traveltime for a ray that travels a distance d in a homogeneous medium with elliptical anisotropy and the axis of symmetry forming an angle γ with respect to the vertical (Figure 1.1) is

$$t = \sqrt{\frac{(\Delta x \cos\gamma + \Delta z \sin\gamma)^2}{V_\perp^2} + \frac{(-\Delta z \cos\gamma + \Delta x \sin\gamma)^2}{V_\parallel^2}}, \tag{1.1}$$

where $\sqrt{\Delta x^2 + \Delta z^2} = d$, and $V_\parallel$ and $V_\perp$ are the velocities in the directions parallel and perpendicular, respectively, to the axis of symmetry. Appendix **??** explains how to derive this expression.

If the model is described as a superposition of N homogeneous orthogonal regions, the traveltime for the i^{th} ray traveling across the j^{th} region is

$$t_{i,j} = \sqrt{\frac{(\Delta x_{i,j} \cos\gamma_j + \Delta z_{i,j} \sin\gamma_j)^2}{V_{\perp_j}^2} + \frac{(-\Delta z_{i,j} \cos\gamma_j + \Delta x_{i,j} \sin\gamma_j)^2}{V_{\parallel_j}^2}}. \tag{1.2}$$

Note that each homogeneous region is characterized by three parameters: two velocities and the angle of the axis of symmetry with respect to the vertical. From here on I refer to these parameters as interval parameters. In the preceding equation,

Figure 1.1: Ray traveling a distance d in a medium with a tilted axis of symmetry. α and γ are the angles (positive counterclockwise) of the ray and the axis of symmetry, respectively, in relation to the vertical. ray-and-axis [NR]

$\sqrt{\Delta x_{i,j}^2 + \Delta z_{i,j}^2}$ is the distance traveled by the i^{th} ray in the j^{th} cell. The sum of expressions like equation (1.2) can be used to compute the traveltime from source to receiver for a ray that travels in a heterogeneous medium, assuming that the ray path is known. In chapter 3, I explain how to do the anisotropic ray tracing.

Figure 1.2 shows an example of the type of model I consider in this chapter. It consists of homogeneous elliptically anisotropic blocks separated by straight interfaces with variable dip (a_j) and intercept (b_j). I assume that all axes of symmetry of the different layers lie in the plane of the survey. If $\Delta x_{i,j}$ and $\Delta z_{i,j}$ are defined as

$$\Delta x_{i,j} = x_{i,j+1} - x_{i,j}, \tag{1.3a}$$

$$\Delta z_{i,j} = z_{i,j+1} - z_{i,j}, \tag{1.3b}$$

the expression (1.2) for the traveltime $t_{i,j}$ of the i^{th} ray in the j^{th} cell becomes

$$t_{i,j} = \sqrt{{\Delta X_{i,j}}^2 S_{\perp_j}^2 + {\Delta Z_{i,j}}^2 S_{\|_j}}, \tag{1.4}$$

where $S_{\perp_j}$, $S_{\|_j}$, $\Delta X_{i,j}$, and $\Delta Z_{i,j}$ are equal to

$$S_{\perp_j} = \frac{1}{V_{\perp_j}},$$

$$S_{\|_j} = \frac{1}{V_{\|_j}},$$

$$\Delta X_{i,j} = \Delta x_{i,j} \cos\gamma_j + (a_{j+1} x_{i,j+1} + b_{j+1} - a_j x_{i,j} - b_j) \sin\gamma_j,$$

$$\Delta Z_{i,j} = -(a_{j+1} x_{i,j+1} + b_{j+1} - a_j x_{i,j} - b_j) \cos\gamma_j + \Delta x_{i,j} \sin\gamma_j.$$

The point $(x_{i,j}, z_{i,j})$ is the intersection between the i^{th} ray and the j^{th} interface. If the axis of symmetry is vertical ($\gamma_j = 0$), it follows that $\Delta X_{i,j} = \Delta x_{i,j}$ and $\Delta Z_{i,j} = \Delta z_{i,j}$.

Figure 1.2: Model of velocities and heterogeneities. The top and bottom interfaces are horizontal ($a_1 = a_{N+1} = 0$) and located at known depths. This model is neither 1-D nor fully 2-D, but something in between. Therefore, I call it 1.5-D. inv-model [NR]

Besides the interval parameters previously introduced, I have added two more parameters to describe how the boundaries that separate different intervals may change their positions. I call them boundary parameters. Figure 1.2 shows how to count both intervals and boundaries.

The total traveltime for a ray that travels from source to receiver is

$$t_i(\boldsymbol{m}) \;=\; \sum_{j=1}^{N} t_{i,j}(\boldsymbol{m}) \qquad\qquad i = 1, ..., M, \tag{1.5}$$

where $\boldsymbol{m}$ is the vector of model parameters of $5N$ elements:

$$\begin{aligned} \boldsymbol{m} &= (m_1, ..., m_N, m_{N+1}, ..., m_{2N}, m_{2N+1}, ..., m_{3N}, m_{3N+1}, ..., m_{4N}, m_{4N+1}, ..., m_{5N}) \\ &= (S_{\perp_1}, ..., S_{\perp_N}, S_{||_1}, ..., S_{||_N}, \gamma_1, ..., \gamma_N, b_1, ..., b_N, a_1, ..., a_N), \end{aligned} \tag{1.6}$$

and M is the total number of traveltimes. The dimension of $\boldsymbol{m}$ can be reduced if some of the parameters remain fixed during the inversion. For example, if the axes of symmetry are known to be vertical, the components $\gamma_1, ..., \gamma_N$ are not used or if the position of the cells is fixed (e.g., when discretizing the model using square pixels), the parameters $b_1, ..., b_N, a_1, ..., a_N$ are not used either.

Equation (1.5) is the system of nonlinear equations that relates the model parameters to the measured traveltimes. A linearized version of these equations is used in the next section to solve the inverse modeling problem. When the medium is isotropic (i.e., $S_{\perp_j} = S_{||_j} = S_j$), equation (1.5) reduces to the familiar expression that approximates traveltimes computed in an isotropic model (McMechan, 1983):

$$t_i \;=\; \sum_{j=1}^{N} S_j \sqrt{{\Delta x_{ij}}^2 + {\Delta z_{ij}}^2}$$

$$= \sum_{j=1}^{N} S_j d_{ij},$$

where d_{ij} is the length of the i^{th} ray in the j^{th} cell.

1.3 Inverse modeling

In order to understand how to do the decoupling of anisotropy and heterogeneity (when both effects can be separated), let us consider first the case of homogeneous elliptically anisotropic media with a vertical axis of symmetry ($S_\perp = S_x$ and $S_\parallel = S_z$). From studying this case, it is possible to draw some general conclusions about the estimation of velocities that vary with both direction and position.

1.3.1 Homogeneous media

When the model is homogeneous and isotropic, we usually estimate the slowness S of the homogeneous medium that "best" fits the traveltimes by simply averaging all the slownesses S_i obtained from the individual rays as follows:

$$S = \frac{1}{M}\sum_{i=1}^{M} S_i = \frac{1}{M}\sum_{i=1}^{M} \frac{t_i}{l_i}, \tag{1.7}$$

where l_i is the source-receiver distance and M the total number of traveltimes.

When the model is homogeneous and elliptically anisotropic, the two slowness components S_x and S_z that best fit the traveltimes can be obtained by generalizing the average (1.7). This generalization is, as expected, in a least-squares sense. From expression (1.1) we can see that the relation between t^2 and S_x^2 and S_z^2 is linear. Therefore, for a given set of traveltimes and source-receiver locations, it is possible to set up a least-squares problem to find the vector $\boldsymbol{m} = (S_x, S_z)$ of the homogeneous medium. Defining $M_x = S_x^2$ and $M_z = S_z^2$, the least-squares problem is

$$\underset{\sim}{\mathbf{M}} \begin{pmatrix} M_x \\ M_z \end{pmatrix} = \boldsymbol{d}, \tag{1.8}$$

where

$$\underset{\sim}{\mathbf{M}} = \begin{pmatrix} {\Delta x_1}^2 & {\Delta z_1}^2 \\ {\Delta x_2}^2 & {\Delta z_2}^2 \\ \vdots & \vdots \\ {\Delta x_M}^2 & {\Delta z_M}^2 \end{pmatrix},$$

and

$$\boldsymbol{d} = \begin{pmatrix} t_1^2 \\ t_2^2 \\ \vdots \\ t_M^2 \end{pmatrix}.$$

Equation (1.8) can be solved in different ways. The most common approach is to use the normal equations, which results in

$$\begin{pmatrix} M_x \\ M_z \end{pmatrix} = (\underset{\sim}{\mathbf{M}}^T \underset{\sim}{\mathbf{M}})^{-1} \underset{\sim}{\mathbf{M}}^T \boldsymbol{d}. \tag{1.9}$$

However, the normal equations may have undesirable features with respect to numerical stability, because the condition number of $\underset{\sim}{\mathbf{M}}^T\underset{\sim}{\mathbf{M}}$ is the square of the condition number of $\underset{\sim}{\mathbf{M}}$. If $\underset{\sim}{\mathbf{M}}$ is only moderately ill-conditioned, $\underset{\sim}{\mathbf{M}}^T\underset{\sim}{\mathbf{M}}$ is severely ill-conditioned. For this reason, methods that do not amplify the condition number of $\underset{\sim}{\mathbf{M}}$ should be used to solve systems like (1.8) (e.g., QR factorization).

For estimating M_x and M_z *simultaneously* and *accurately*, $\underset{\sim}{\mathbf{M}}$ has to be well conditioned. This is not the case when most of the elements of the matrix satisfy either $\Delta {x_i}^2 \gg \Delta {z_i}^2$ or $\Delta {z_i}^2 \gg \Delta {x_i}^2$. These two inequalities describe cases in which most rays are traveling close to the horizontal or the vertical. In such cases, it is difficult to estimate simultaneously both components of the vector $\boldsymbol{S}$ because the limited view of the measurements results in severe ill-conditioning. This can be understood by trying to estimate M_x and M_z using the simple cross-well experiment shown in Figure 1.3, where $\Delta x^2 \gg \Delta {z_i}^2$. In this case

$$\underset{\sim}{\mathbf{M}} = \begin{pmatrix} \Delta x^2 & \Delta {z_1}^2 \\ \Delta x^2 & \Delta {z_2}^2 \end{pmatrix}.$$

The eigenvalues of this matrix are

$$\lambda_{\pm} = \frac{\Delta x^2 + \Delta {z_2}^2 \pm \sqrt{(\Delta x^2 - \Delta {z_2}^2)^2 + 4\Delta x^2 \Delta {z_1}^2}}{2}.$$

Since $\Delta x^2 \gg \Delta {z_i}^2$, the eigenvalues to the first order are

$$\begin{aligned} \lambda_+ &\approx \Delta x^2 + \Delta {z_1}^2, \\ \lambda_- &\approx \Delta {z_2}^2 - \Delta {z_1}^2. \end{aligned}$$

The largest eigenvalue of $\underset{\sim}{\mathbf{M}}$ is related to the horizontal component of the slowness, and the smallest one is related to the vertical component. In contrast, for a VSP-like geometry, the largest eigenvalue is related to S_z and the smallest one to S_x (Dellinger, 1989). Increasing the number of rays M without increasing the aperture does not solve the problem. In such a case, the largest eigenvalue of the matrix $(\underset{\sim}{\mathbf{M}}^T \underset{\sim}{\mathbf{M}})$ tends to $\sum_{i=1}^{M} \Delta {x_i}^4$ and the smallest one tends to zero again.

Having seen the difficulties of trying to estimate variations of velocity with direction in homogeneous media, let's look at what happens when we try to do the same in heterogeneous media.

1.3.2 Heterogeneous media

When estimating velocities tomographically in heterogeneous media, the goal is to estimate two different sets of coupled unknowns: the model parameters and the ray

Figure 1.3: Cross-well experiment with two rays. experiment [NR]

paths. The usual way to decouple them is by invoking Fermat's principle, which "justifies" the trick of assuming one to estimate the other in an iterative fashion, as long as the magnitude of the changes from one step to the next are kept small.

Once we have estimated the ray paths, we need to solve the system of nonlinear equations (1.5) in order to find a new model in which rays are again traced. One way to solve (1.5) is as a sequence of linearized steps starting from a given initial model $\boldsymbol{m}_\circ$. The first step is to approximate such an equation by its first-order Taylor series expansion centered about a given model $\boldsymbol{m}_\circ$:

$$\begin{aligned} t_i(\boldsymbol{m}) &\approx t_i(\boldsymbol{m}_\circ) + \nabla t_i(\boldsymbol{m}_\circ) \cdot (\boldsymbol{m} - \boldsymbol{m}_\circ) \\ &= t_i(\boldsymbol{m}_\circ) + \sum_{n=1}^{5N} \underset{\sim}{\mathbf{J}}_{in} (m_n - m_{0n}), \end{aligned} \tag{1.10}$$

where the elements of the Jacobian $\underset{\sim}{\mathbf{J}}_{in}$ are

$$\underset{\sim}{\mathbf{J}}_{in} = \left. \frac{\partial t_i}{\partial m_n} \right|_{\boldsymbol{m}=\boldsymbol{m}_\circ}.$$

The explicit forms of these derivatives are given in appendix **??**. In contrast with the Jacobian for the isotropic case, the matrix $\underset{\sim}{\mathbf{J}}$ when the medium is anisotropic depends *explicitly* on the interval parameters of the reference model $\boldsymbol{m}_\circ$. In the isotropic case, the Jacobian depends only on the lengths of the rays at each pixel, and, therefore, when the rays are straight the estimation of slowness becomes a linear

problem because the Jacobian is constant. In the anisotropic case, however, the problem is still nonlinear even if the rays are straight. Ray bending introduces an additional type of nonlinearity into the problem.

If we assume that $t_i(\boldsymbol{m})$ represents one component of the vector $\boldsymbol{t}$ of measured traveltimes, we can compute the perturbations $\Delta\boldsymbol{m}_n = (m_n - m_{0n})$ once the traveltimes in the reference model $\boldsymbol{m}_0$ have been calculated. The perturbation $\Delta\boldsymbol{m} = (\boldsymbol{m} - \boldsymbol{m}_0)$ is the solution of the following system of equations:

$$\underset{\sim}{\mathbf{J}}\,\Delta\boldsymbol{m} \;=\; \Delta\boldsymbol{t}, \tag{1.11}$$

where $\Delta\boldsymbol{t}_i = t_i(\boldsymbol{m}) - t_i(\boldsymbol{m}_0)$. In practice, only a fraction r of the correction $\Delta\boldsymbol{m}$ is added to the given model:

$$\boldsymbol{m}_1 = (\boldsymbol{m}_0 + r\Delta\boldsymbol{m}),$$

where r (the step length) is usually kept small to avoid large changes in the ray paths from one iteration to the next.

In appendix **??**, I compute the singular value decomposition (SVD) of the matrix $\underset{\sim}{\mathbf{J}}$ for the following models with fixed interfaces: 1-D isotropic, 1-D anisotropic, 2-D isotropic and 2-D anisotropic. The results are roughly a combination of the results I derived in the section "Homogeneous media" and the results previously published for isotropic heterogeneous media (Bregman et al., 1989; Pratt and Chapman, 1992); that is, the more sensitive part of the model related to the largest singular values of the Jacobian, corresponds roughly to vertical variations in the horizontal component of the slowness, whereas the less sensitive part of the model corresponds to horizontal and high-frequency variations in the vertical component of the slowness. As a consequence, in two dimensions, S_x and S_z cannot be estimated with the same resolution because a large part of the variations in S_z are in the null space of the problem. In one dimension, S_x and S_z can be estimated with the same resolution only when the smallest singular values of the problem can be also retrieved. The last section of this chapter shows examples that illustrate this issue.

Based on the observations derived from the SVD that estimating anisotropy and heterogeneities in 1-D models is by far an easier problem than in 2-D models, I consider intermediate models like the one shown in Figure 1.2 where the only type of lateral variations allowed in the model are as straight interfaces with variable dip and intercept.

In the examples shown later, the system of linear equations (1.11) is solved using the LSQR variant of the conjugate gradients algorithm (Nolet, 1987), which has been proved to be faster than SIRT methods (Nolet, 1985; Van der Sluis and Van der Vorst, 1987).

1.3.3 Constraints

Prior information about the real medium can be introduced in the inversion in two ways: with the starting model and with bounds on the variations of the parameters

being estimated. In this particular algorithm, both these forms of prior information are *essential* for a reliable estimation of the vector $\boldsymbol{m}$.

If the starting model is "far" from the "true" answer the algorithm may not converge at all, or, if it does, it may produce a wrong answer. Although this problem may happen with any nonlinear inversion, it can be shown that if the starting model is "close" to the true answer, a linearized solution of the nonlinear system of equations (1.5) converges quadratically (Gill et al., 1981). Therefore, any information introduced in the initial model (especially about dips) helps the algorithm converge to a more reliable estimate of the actual medium.

When the interfaces are allowed to change position from one iteration to the next, the algorithm has to ensure that each new model does not contain crossing interfaces in the area of interest. If two interfaces cross after adding $r\Delta\boldsymbol{m}$ to the given model, the step length r is reduced until those interfaces do not cross after the correction. Once the model is updated and no crossing interfaces are found, the algorithm checks whether thin layers have been created or not, and, if so, those layers are eliminated from the inversion, reducing by a multiple of five the number of model parameters (five parameters for each layer eliminated). The layers are eliminated by comparing their thicknesses with a predetermined minimum layer thickness, as long as the corresponding boundaries are parallel (also within a predetermined range of angles). If the predetermined minimum thickness is too small, the solution may contain layers with artificially high (or low) velocities, and if the minimum is too big, spatial resolution in the model may be lost.

Whenever information is available about the position and dip of certain layers of the medium (from well logs, for example) it should also be used to constrain the corresponding interfaces in the model.

When appropriate, especially in 2-D models, the solution should also be required to be smooth.

1.3.4 Which is the axis of symmetry?

Every ellipse has two axes of symmetry. The inversion algorithm proposed in this chapter can estimate the inclination with respect to the vertical of either one, depending on which axis is closer to the vertical in the initial model. In either case, the estimated parameters describe the same *elliptical velocity function*.

Another way to understand why the inversion can estimate the inclination of either axis of symmetry is to examine the traveltime equation (1.1). We can obtain an identical equation if in (1.1) we switch $V_{||}$ and $V_{\perp}$, changing at the same time γ by $\gamma \pm \pi/2$. This means that the traveltimes are affected only by the elliptical function of velocities, regardless of how such a function is described. Figure 1.4 shows how a given ellipse can be described with two different sets of parameters.

If the inversion procedure is constrained to estimate the same axis of the ellipse (either the major or the minor) for every layer, it can be more difficult (or impossible)

Figure 1.4: The same ellipse represented in two different ways by interchanging $V_\perp$ and $V_{||}$ and rotating the axis of symmetry $-\pi/2$. Traveltimes are affected by the velocity function (elliptical in this case) regardless of how that function is described. two-sets [NR]

to get a reliable estimate of the real elliptical velocity function of the medium, especially in cases when the axis of symmetry in the initial model is far from the actual axis of symmetry.

Because of this property of ellipses, it is easier for the algorithm to estimate inclinations of axes of symmetry close to the vertical or close to the horizontal than intermediate inclinations that are not close to either axis.

1.4 Synthetic examples

In this section, I show the application of the inversion algorithm just described in different situations that demonstrate its advantages and weaknesses when used to invert cross-well traveltimes. First, I consider the case of traveltimes generated in a 1-D isotropic model that are inverted using a 1-D anisotropic model with fixed boundaries and vertical axes of symmetry. This first example, which can be considered a linear inversion because the velocity variations are nearly one percent, illustrates several issues related to the convergency of the algorithm. Second, I show what happens when the assumption of layering is relaxed and a full 2-D anisotropic inversion is performed with data generated in a weakly varying 2-D isotropic model. Finally, I show an example of the inversion that uses the intermediate 1.5-D model shown in Figure 1.2. Unlike the first two examples, the final example doesn't assume either weak heterogeneity or weak anisotropy, and the orientation of the axis of symmetry varies through the model. All the models are assumed to be elliptically anisotropic.

Chapter 5 addresses the more general case of transversely isotropic models.

1.4.1 1-D inversion

Synthetic data were generated through the 1-D isotropic model shown in Figure 1.5, using a geometry of 17 sources and 17 receivers equally spaced at the source and receiver well, respectively.

Figure 1.5: 1-D isotropic model used to test the algorithm. At the right, the two components of the slowness are plotted one after the other. They represent the slowness vector that describes this model. The first half of the vector corresponds to the horizontal component and the second half to the vertical. syn-model1 [NR]

The inversion is constrained by allowing only vertical variations in the model.

This constraint eliminates instabilities and nonuniqueness in the inversion associated with lateral variations, retaining only those variations associated with the vertical component of the slowness, which is not sampled sufficiently by the cross-well recording geometry. The constraint also reduces the dimension of $\boldsymbol{m}$ to $2N$ instead of $5N$. I call the reduced vector $\boldsymbol{S}$, instead of $\boldsymbol{m}$, to suggest that it only contains information about the slownesses at each layer, and not about the positions of the boundaries and orientations of the axes of symmetry.

If we plot components of the slowness vector $\boldsymbol{S}$ [equation (1.6)] for this model, we obtain the profile shown at the right side of Figure 1.5. Both slowness components are identical because the model is isotropic. In this example, the slowness contrast between the background and the anomalous layer is small (one percent), and therefore the propagation of the energy can be safely modeled by straight ray paths.

The image area was divided into 100 layers of equal thickness (8 feet). The inversion process has to estimate 200 parameters from 289 traveltimes. Figure 1.6 shows the slowness vector obtained after 60 conjugate gradients (CG) iterations. There is no difference between the given $\boldsymbol{S}$ (Figure 1.5) and the estimated one (Figure 1.6). Note that the results can be represented either as a function of depth or as a function of the index of the slowness vector. In the two next results the depth axis is omitted.

Figure 1.6: Result of the inversion of the synthetic data generated with the model shown in Figure 4.5. The first half of the curve corresponds to the horizontal component of slowness and the second half to the vertical component. 1d-synthetic [NR]

Figure 1.7 shows how the algorithm converges toward the answer as a function of the CG-iterations. The result shown in Figure 1.6 corresponds in Figure 1.7 to 60 CG-iterations along the axis *cg iterations*. The two "hills" represent the slowness at

Figure 1.7: Variations of the slowness vector as a function of the number of conjugate gradient iterations. The original model is shown at the top. The axes "i" and "cg

the anomalous layer. Convergence is achieved when the top and the bottom of the hills are flat for an increasing number of CG-iterations. The horizontal component of the slowness converges faster than the vertical component. This is because in the given model the horizontal component of the slowness in the anomalous layer is better sampled than the vertical component: the range of ray angles (absolute values) is from 0 to 53 degrees [$53 \approx \arctan(\frac{800}{600})$], which is a typical range for cross-well experiments. Because of this bias of cross-well geometries toward the horizontal, the largest singular values of the problem (1-D anisotropic) are related to the horizontal component of the slowness, as appendix **??** shows.

When synthetic data is generated through the model shown at the top of Figure 1.8 (where the well-to-well separation is shorter), both components converge at the same rate. This is because the vertical component of the slowness is better sampled in this example because the range of ray angles is wider. The angles vary between 0 and 76 degrees [$76 \approx \arctan(\frac{800}{200})$].

The preceding results tell us that if it is not possible to do "enough" CG-iterations in order to reach the flat top of both hills (Figures 1.7 and 1.8), we may wrongly conclude that the medium is anisotropic because components of the slowness in different directions may converge with different speeds. Severely limited view problems as well as low signal-to-noise ratios are some of the factors that may limit the amount of CG-iterations that can be performed before the smallest singular values of the problem start affecting the solution.

1.4.2 2-D inversion

To test the performance of the algorithm in inverting data generated in a 2-D model, I computed synthetic traveltimes through the isotropic model shown in Figure 1.9. The separation between contiguous sources and receivers is 10 feet. Each receiver gather only uses sources located at ± 50 degrees from the horizontal. With a geometry like this, I simulate the geometry of a field data examples to be analyzed later. As in the previous example in 1-D, the slowness contrast between the anomaly and the background is small (five percent), and therefore straight rays can be used again.[1]

The unknown model was discretized in 241×46 pixels (5×5 ft^2 each), and therefore

[1]My implementation of the anisotropic ray tracing algorithm described in chapter 3 is not valid for 2-D anisotropic models described as a superposition of square pixels. However, if the rays are assumed to be straight because of small velocity contrasts, tracing rays in elliptically anisotropic models is reduced to computing the corresponding traveltimes by using equation 4.5.

Figure 1.8: Variations of the slowness vector as a function of the number of conjugate gradient iterations. The only difference between the model shown at the top and the

Figure missing !

Figure 1.9: 2-D isotropic slowness model. The radius of the circular anomaly is $r = 50$ and is centered at $(100, 700)$. The background slowness is 1.0, and the slowness of the disc is 1.05. s-model-test [NR]

the inversion has to estimate $241 \times 46 \times 2$ parameters from 2200 synthetic traveltimes. Figure 1.10 shows the results of the inversion. The slowness of the isotropic circular anomaly is better estimated by the horizontal than by the vertical component of the slowness in the anisotropic model This is not the case in the 1-D inversion, where both slowness components can be perfectly recovered even though the vertical component of the slowness is not properly sampled. The extra information introduced in that problem by assuming that the model is layered compensates for the limitations produced by the limited view of the measurements. In the 2-D inversion, where the unknowns are less constrained, the better sampling of the horizontal component results in its better recovery when compared with the vertical component and, as a consequence, artificial anisotropy is introduced by the reconstruction. In this noise-

free example such anisotropy is not greater than three percent, as the ratio $\frac{S_z}{S_x}$ in Figure 1.10 shows. Doing more CG-iterations does not help to reduce this artificial anisotropy to zero, as in the 1-D inversion (Figures 1.7 and 1.8). This is because S_z contains more information than S_x in the null space, as I show in appendix **??**. In the present case the images did not change after 120 CG iterations.

Figure 1.10: Reconstructed horizontal and vertical component of the slowness. The ratio of the two components at the right shows the artificial anisotropy introduced by the reconstruction. Ideally, in this isotropic model, the ratio of slownesses should be unity everywhere. sx2d-test [NR]

This example shows that when the velocity contrasts are small, the anisotropy introduced by the inversion can be of the same order as the expected heterogeneities. The artifacts in both slowness components are similar to the well-known truncation artifacts in isotropic inversion, although they are different from one component to

the other. Rays that travel horizontally do not influence significantly the estimation of S_z as they do the estimation of S_x. Therefore, the estimated S_x is smeared along the horizontal direction whereas S_z is not. When data from only one geometry are used, the different character of the artifacts for each slowness component can limit our ability to recover variations in actual anisotropy at the same resolution of variations in velocity. This difficulty is apparent in the application to field data later in this chapter.

Since the inversion algorithm introduces anisotropy in the results when the model is fully 2-D, it may be difficult to separate small variations in anisotropy from reconstruction artifacts. If the anisotropy is too weak, it may fall below the level of noise of the reconstruction artifacts and be unable to be reliably estimated. Therefore, when the heterogeneities are described as a superposition of orthogonal square pixels, algorithms based on the weak anisotropy assumption (Stewart, 1988; Chapman and Pratt, 1992; Lines, 1992; Williamson et al., 1993) will produce reliable estimates of anisotropy only if the actual anisotropy is not too weak.

1.4.3 1.5-D inversion

In this example, 4992 traveltimes were generated through the model shown in Figure 1.11 for a geometry where sources were located within ± 45 degrees with respect to the horizontal at each receiver position. I used the anisotropic ray tracing algorithm described in chapter 3 to compute the synthetic traveltimes and to trace the rays needed in the nonlinear inversion. The starting model used for the inversion was homogeneous isotropic described by 17 horizontal layers of equal thickness. The inclination used for the axis of symmetry was $\gamma = 0$ in all layers. Figure 1.12 shows the initial positions of the boundaries in the starting model. By starting the iterations with this model, I wanted to test how the interfaces arranged themselves to create a dipping layer not present in the initial model.

The inversion was constrained by not allowing parallel layers (within ± 5 degrees) to be thinner than 15 feet. No smoothing was applied to the model after each iteration.

Figure 1.13 shows the result of the inversion after tracing rays 35 times, with few conjugate gradient iterations between each ray tracing. The boundaries have moved with respect to their initial positions, and the initial 17 layers have been reduced to 10 to allow the positioning of the dipping layers at the correct depths with the correct dips. The inclinations of the axes of symmetry estimated by the algorithm are also correct. Figure 1.14 compares profiles at $x = 0$ of the real model (Figure 1.11) and the estimated one (Figure 1.13). The agreement is almost perfect.

In this example it was possible to estimate correctly both small and moderate dips (between 0 and 30 degrees), but the answer to the question about the maximum and minimum dips that can be retrieved from the data depends in general on the aperture of the recording geometry, the interval between sources and receivers, and the frequency of the data.

Figure 1.11: 1.5-D model used to test the inversion. The third interface dips 15 degrees and the fourth one -30. The inclination of the axis of symmetry in the second layer is -15 degrees and 40 degrees in the fourth layer. The ratio $\frac{V_\perp}{V_\parallel}$ at the fourth layer is 1.26. The gray scale shows variations in velocity. "$V+$" stands for $V_\perp$, "$V||$" for $V_\parallel$, and "gamma" for γ. syn-model [NR]

Figure 1.12: Initial position of the interfaces in the starting model (homogeneous isotropic). The velocity is equal to 12 000 ft/sec, and the inclination of the axes of symmetry with respect to the vertical is zero for all layers. initial-model-syn [NR]

1.5 Field data examples

Anisotropic traveltime tomography was also performed with cross-well P-wave traveltimes recorded at an Amoco Gulf Coast site and BP's Devine test site.

At these two sites, the wells are not confined to a single plane. Instead, they deviate gradually from the vertical plane that contains them at the near surface. I have taken this effect into account by following this two-step procedure:

1. Find the true 3-D distances between sources and receivers.
2. Assume that one well is vertical (for example, the source well) and locate the receivers at the corresponding true relative distances and true depths in the other well, which is equivalent to locating the origin of the coordinates to measure the distances at the source well.

When correcting for the well deviation in this way, actual source-receiver separations are used in the inversion.

To measure the closeness between measured and calculated traveltimes, I use the mean

Figure 1.13: 1.5-D anisotropic inversion. Notice how the interfaces have changed their initial positions. The position of each arrow's head shows the interval that corresponds to each γ. The gray scale shows variations in velocity. final-model-syn [NR]

Figure missing !

Figure 1.14: Profile at $x = 0$ of the real model and the estimated one (Figures 4.11 and 4.13, respectively). The continuous line represents the real model; the dashed one represents the result of the inversion. The agreement between real and estimated parameters is almost perfect. final-model-profile-syn [NR]

absolute value of the residuals

$$error \;=\; \frac{1}{M}\sum_{i=1}^{M} |t_{c_i} - t_{r_i}|, \tag{1.12}$$

where t_{r_i} and t_{c_i} are the measured and calculated traveltimes, respectively, and M is the total number of traveltimes.

When the real velocities are elliptical, the direct velocity along one axis and the normal moveout (NMO) velocity around the perpendicular axis are equal. For this reason, no distinction was made between direct and NMO velocities in the synthetic examples of the previous section. In field data applications, however, such a distinction needs to be made because in general the rocks are not elliptically anisotropic. Therefore, after doing anisotropic traveltime tomography with a given data set, we

must label the velocities appropriately (either direct or NMO) before procceding to estimate the elastic constants of the medium as explained in chapter 2. Moreover, even if the mapping to elastic constants is not possible because the data set is incomplete, we should still label the velocities correctly before interpreting the results.

1.5.1 Gulf Coast site

Cross-well data were acquired jointly by Amoco Production Company and Stanford University at an on-shore Gulf Coast site in Southeast Texas. The overall survey geometry is illustrated in Figure 1.15. This geometry is similar to the one used in the synthetic example of 2-D inversion. The source, a piezoelectric bender bar, produced a sweep signal with frequencies between 400 Hz and 1600 Hz. The data were recorded with a sample interval of 0.1 msec. More details about the site and geometry are found in Harris et al. (1990).

Nearly 5000 P-wave first arrival times were picked from the correlated data. In general, I found that the traveltimes corresponding to the near horizontal rays (or near vertical offsets) were more difficult to pick than those at far offsets.

Because the shots are within ± 50 degrees with respect to the horizontal at each receiver location, we can expect most of the data to be modeled appropriately using elliptical anisotropy, as I show in chapter 2 by fitting a P-wave impulse response with ellipses estimated from data at different apertures, up to 40 degrees.

The relative position of the two wells, taking into account the deviation, is shown in Figure 1.16. To use the true relative distances, it is necessary to move the receiver positions horizontally in the deviated well. For this reason, the receiver positions in Figure 1.16 look slightly smeared in the horizontal direction. The selection of the vertical well used as a reference to measure the relative deviations is irrelevant if we assume that the model is 1-D. In two dimensions different distorsions may occur depending on which well is chosen as a reference and how strong the actual 2-D variations are.

1-D inversion

The simplest inversion that we can possibly do assumes a homogeneous isotropic model. The result is the mean velocity [equation (1.7)], $V_{iso} = 8452$ ft/sec. The next step is to assume that the model is still homogeneous but elliptically anisotropic. Using equation (1.8) I found that $V_x = 8586$ ft/sec and $V_{z\text{NMO}} = 8079$ ft/sec.[2] For this particular recording geometry (Figure 1.15), V_{iso} is closer to V_x than to $V_{z\text{NMO}}$, which means that the "averaging" of the horizontal and vertical directions that the isotropic inversion implicitly

[2]Since only P-waves are used in the field data examples of this chapter, I have omitted the "P" when talking about $V_{P,x}$ and $V_{P,z\text{NMO}}$.

Figure 1.15: Overall survey geometry illustrating the shooting pattern. Receivers are spaced at $dr = 10$ feet between 2688 and 3996 feet. Sources are spaced at $ds = 10$

Figure 1.16: Positions of the source and receiver wells plotted after considering their relative deviations. Each dot represents a source or a receiver position (left and right respectively). The density of sources is larger at the middle of the surveyed area than at the extremes. deviation [NR]

does is not a simple arithmetic average. As I show later, the same conclusion can be drawn when the model is heterogeneous.

The mean absolute value of the residual [equation (1.12)] for the homogeneous isotropic model is 1.04 ms. When the model is homogeneous anisotropic, $error = 0.94$ ms.

Figure 1.17 shows the result of the isotropic inversion when the model is one dimensional. The traveltimes used correspond to rays below 2705 feet and above 4000 feet. This depth interval was discretized in 60 horizontal layers of equal thickness (21.583 feet). Straight rays were used to compute synthetic traveltimes since, according to Harris et al. (1990), small velocity variations are expected in this site. The 2-D isotropic, straight-ray tomogram shown in a later subsection is similar to the 2-D isotropic, curved-ray tomogram obtained by Harris et al. (1990). I did conjugate gradient iterations (40) until no appreciable changes were seen either in the model or in the error (1.12), which is equivalent to reaching the flat part of the hills in Figure 1.7. For the model shown in Figure 1.17, $error = 0.67$ ms.

Then, I allowed the 1-D model to be anisotropic. Figure 1.18 shows the result of the

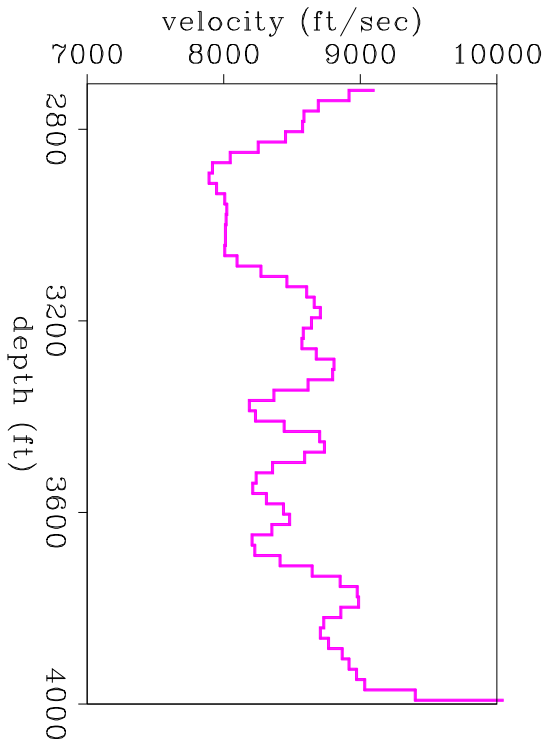

Figure 1.17: 1-D isotropic inversion. The thickness of each layer is 21.583 feet. Isos [NR]

inversion. For traveltimes computed through this model, *error* = 0.59 ms. The thick curve represents the horizontal velocity, and the thin one represents the vertical NMO velocity. The first thing one notice is that V_x is generally larger than $V_{z\text{NMO}}$. Figure 1.19 compares V_x and $V_{z\text{NMO}}$ with V_{iso}. In general, V_{iso} is closer to V_x than it is to $V_{z\text{NMO}}$, which is consistent with the previous results of the inversion assuming a homogeneous medium. This means that for the type of recording geometry used (ray angles between 0 and ± 50 degrees) the isotropic inversion is affected primarily by the horizontal component of the velocity. Since there are fewer rays at large angles, the isotropic inversion is less constrained by them.

At this site, sonic logs were available at both wells (Figure 1.20). Sonic logs sample the vertical component of velocity a few inches away from the well, at frequencies ($\sim$ 10 kHz) much larger than the typical frequency of the cross-well data ($\sim$ 1 kHz). To compare the information obtained from these two types of measurements (1-D tomogram and velocity logs), I did some averaging to the logs. First, I averaged each slowness log in blocks of thickness equal to the layer thickness in the 1-D tomographic inversion. I then averaged

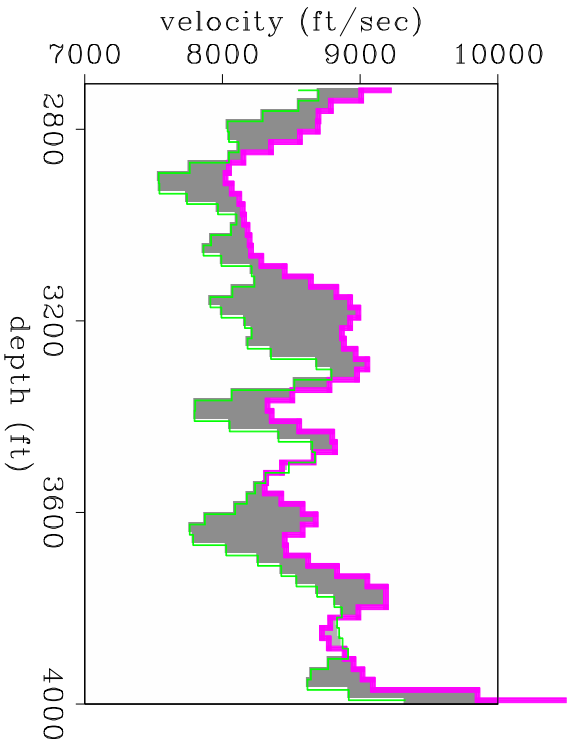

Figure 1.18: 1-D anisotropic inversion. The thickness of each layer is 21.583 feet. The differences between V_x (thick line) and $V_{z\mathrm{NMO}}$ (thin line) are represented by two colors: light gray when $V_x > V_{z\mathrm{NMO}}$, and dark gray when $V_x < V_{z\mathrm{NMO}}$. Anisxsz [NR]

the two averaged slowness logs into a single one. The purpose of the last averaging was to produce a single curve to compare with the $V_{z\mathrm{NMO}}$ estimated by the inversion algorithm. Figure 1.21 compares the average velocity log with V_{iso}, V_x, and $V_{z\mathrm{NMO}}$. When compared with V_{iso} and V_x, $V_{z\mathrm{NMO}}$ is not only much closer to the average sonic velocity but also better correlated with it. Figure 1.21 shows that assuming an elliptical model for the velocities is an improvement over assuming a circular, that is, isotropic one.

The comparison between the average sonic velocity and $V_{z\mathrm{NMO}}$ has to be interpreted carefully, because each curve averages the medium velocities in a different way where the medium changes laterally. On the one hand, the average log assumes that at each depth the medium has only two velocities that contribute with equal weight to the estimate (mean). On the other hand, the way the inversion averages the lateral changes in the medium properties when computing $V_{z\mathrm{NMO}}$ is not clear at this point. It is also not clear at this point how the potential errors of inverting for 1-D variations in a 2-D medium propagate into the solution. Some parts of the real medium show lateral variations, which becomes evident when performing the 2-D inversion.

Figure 1.21 also shows that $V_{z\mathrm{NMO}}$ is systematically larger than the log velocity V_z, which is just the opposite of what I expected from (**??**), if the anisotropy is assumed to be caused by fine layering. In a later section, I explain different sources of biases in the inversion that may explain this result.

The ratio $V_x/V_{z\mathrm{NMO}}$ is roughly correlated with the lithology, as shown in Figure 1.22. In this figure, the thick line corresponds to the ratio $V_x/V_{z\mathrm{NMO}}$, and the

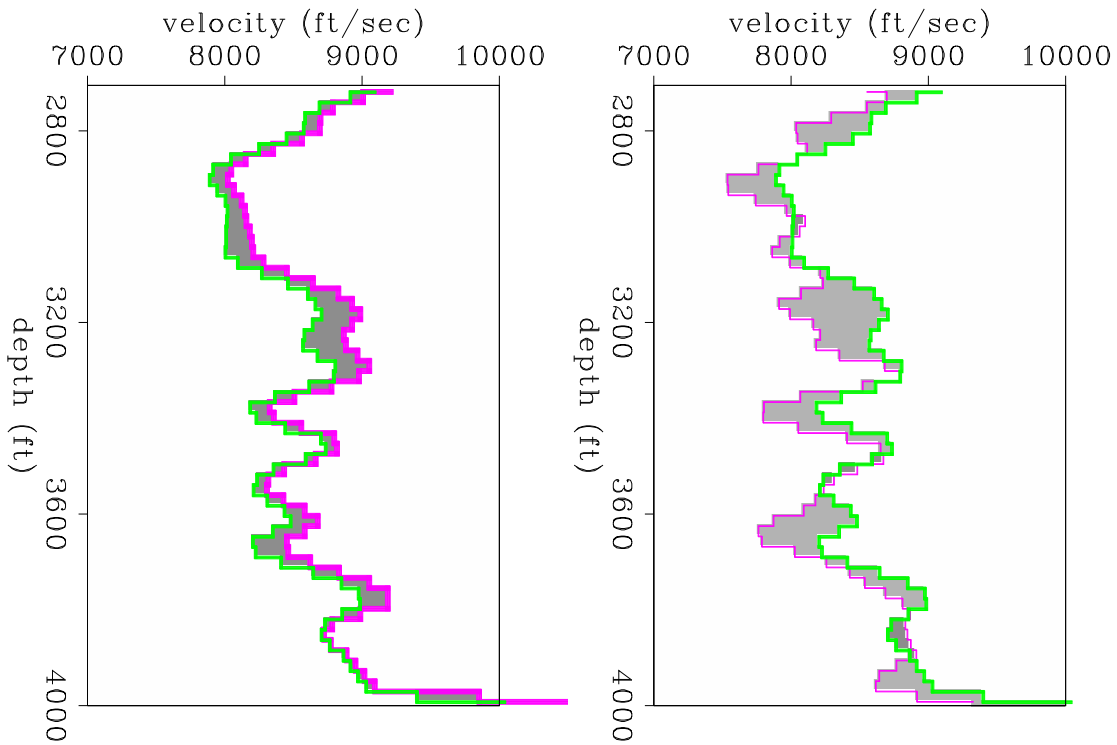

Figure 1.19: Comparison between isotropic and anisotropic layered inversion. Left: V_{iso} (thin line) and and V_x (thick line). Right: V_{iso} (thick line) and $V_{z\text{NMO}}$ (thin line). The differences between the isotropic and anisotropic inversion are represented by two colors: light gray when $V_{iso} > V_x$ or $V_{z\text{NMO}}$, and dark gray when $V_{iso} < V_x$ or $V_{z\text{NMO}}$. IsosAnisxsz [NR]

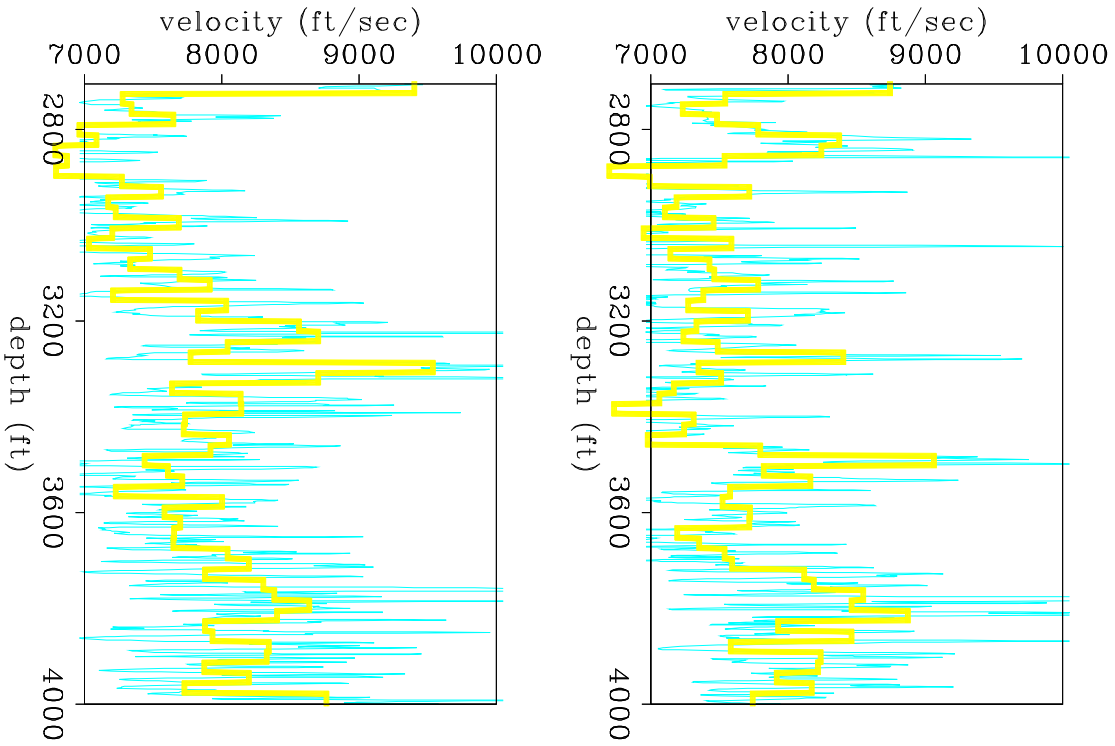

Figure 1.20: Sonic logs at the source well (left) and receiver well (right). The thin line represents the original log. The thick line represents the corresponding log averaged in 60 layers of equal thickness (21.583 feet). two-logs [NR]

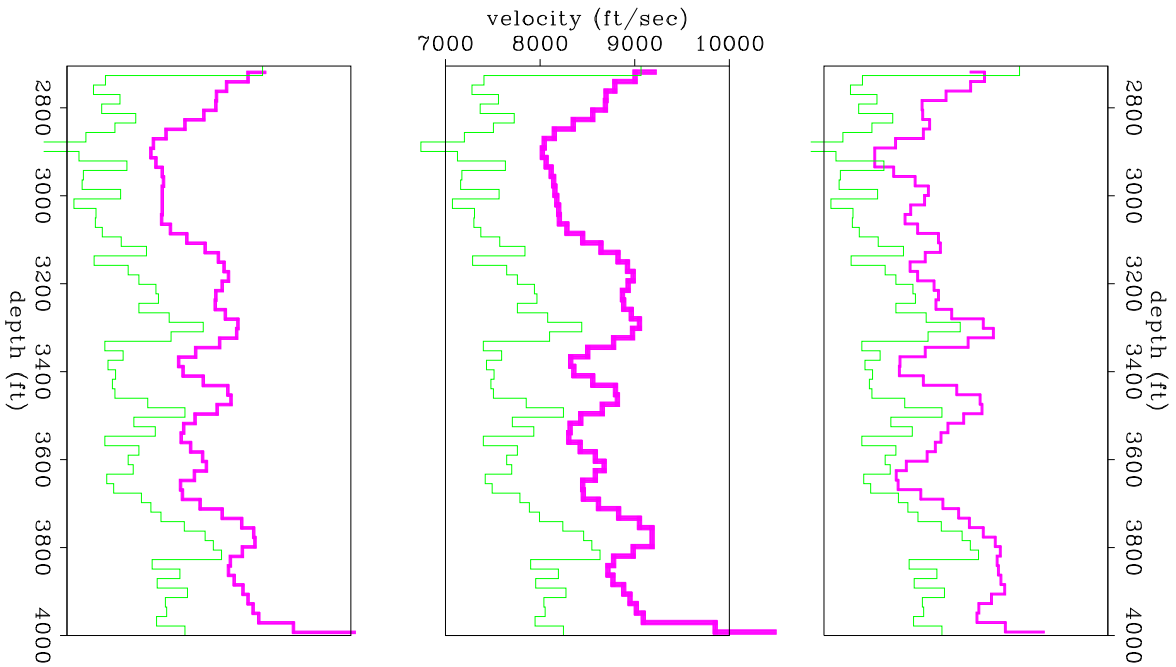

Figure 1.21: Average velocity log (V_z) compared with V_{iso} (left), V_x (center), and $V_{z\text{NMO}}$ (right). $V_{z\text{NMO}}$ is closer and better correlated with the velocity log. logs-vs-veloc [NR]

thin one corresponds to the average spontaneous potential (SP) log. The average SP log was obtained by blocking each log separately, taking the average of the results, and removing a linear trend with depth in the final average. There is a good correlation between large SP values (that indicate the presence of shales) and large anisotropy ratio. The same happens for low SP values (sands) and isotropic layers. When interpreting these results, however, we must keep in mind that each curve represent a different type of average of the lateral changes in medium properties.

In the anisotropic inversion of this data set, in order to reach a good compromise between resolution and stability, I used 60 layers of 21.583 feet each. Reducing the layer thickness by half has the effect (not shown) of increasing the resolution at the expense of

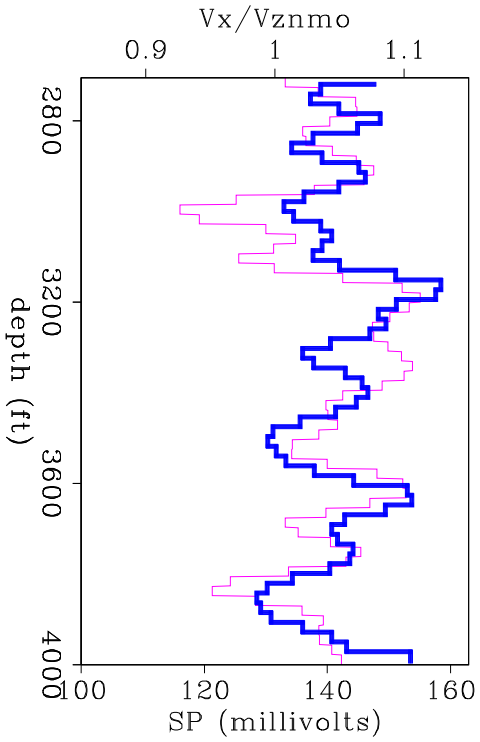

Figure 1.22: Anisotropy ratio $V_x/V_{z\mathrm{NMO}}$ (thick line) compared with the SP log (thin line). SP-Ani [NR]

large variations and instabilities in the vertical component of the velocity that is not well sampled by the recording geometry. The horizontal component of velocity is generally more stable than the vertical for smaller layer thicknesses. Obviously, at the expense of resolution, increasing the layer thickness made the inversion more stable.

2-D inversion

When the relationship between the data and the unknown is linear, we should obtain the model that best fit the data in only one solution of the ray tracing problem. When the problem is nonlinear one approach is to solve it as a sequence of linearized steps. We usually call these steps *external* iterations, to differentiate them from the *internal* iterations needed to solve each linear problem when using iterative techniques such as conjugate gradients. Ideally, if the problem has n unknowns, each external iteration should consist of m CG-steps (m internal iterations), where $m \leq n$ is the number of different singular values. When dealing with field data, however, we might not be able to take that many steps because of the presence of the noise. Noise can affect the solution of each linearized problem in the following ways: (a) it might be amplified into the model by the smallest singular values recovered when m iterations are performed, and (b) it might considerably affect the accuracy of the search directions and, consequently, the position of the minimum associated with the solution. Therefore, we have to deal carefully with the noise.

Under the straight-ray assumption, only one external iteration was needed in the

1-D inversion to find the model shown in Figure 1.18. By selecting the layer thickness appropriately, I was able to do the CG-iterations required to reach convergency without being much affected by the noise. Thicker layers damped the solution, whereas thiner layers introduced instabilities. In two dimensions, however, the situation is different. I found here that the results were more sensitive to noise in the data than the 1-D solutions. This is not surprising because in two dimensions, as explained in appendix **??**, we are trying to estimate high-frequency variations in $S_{z\text{NMO}}$, which are related to the smallest singular values of the problem that amplify the noise.

Because of the sensitiveness to the noise of the 2-D inversion, it is necessary to avoid doing "many" CG-iterations at each linearized step. After doing several tests that combined in different ways external and internal iterations with mean-average smoothing of the slowness model, I adopted a conservative approach to minimize the error (1.12). The approach consisted of the following steps:

1. Compute traveltimes in the given model, calculate the matrix $\underset{\sim}{\mathbf{J}}$, and find the residuals.

2. Approximate the solution of the linear problem (1.11) by applying a few (typically one or two) CG-iterations. Limiting the number of CG-iterations is, for practical purposes, equivalent to damping (Scales and Gersztenkorn, 1988).

3. Smooth the updated slowness model.

4. Repeat the preceding steps until there is no reduction in the sum (1.12). When this happens, either stop the process or increase the number of CG-iterations by one and check whether further reductions in the residuals are obtained.

When the problem is linear, the solution is not obtained in only one iteration because of the presence of the noise.

When the previous procedure was applied to estimate an isotropic model from the data, I obtained the image shown in Figure 1.23 ($error = 0.54$ ms). In this case, the unknown model was discretized into 131×26 square cells (10×10 ft^2 each). It is interesting to note that adding more degrees of freedom to describe the heterogeneity (i.e., more cells) does not substantially improve the parameter *error* obtained with 28 times fewer degrees of freedom in the 1-D anisotropic inversion. The model shown in Figure 1.23 is similar to the one obtained by Harris et al. (1990), where ray bending has been taken into account.

The result of the 2-D anisotropic inversion is shown in Figure 1.24 ($error = 0.45$ ms). As in the 1-D example, that V_x is remarkably similar to V_{iso}. The main difference between these two images is that in V_x (Figure 1.24) the events tend to be more horizontally smeared than in V_{iso} (Figure 1.23). This result was predicted from the 2-D synthetic example shown in Figure 1.10.

Since V_z is not adequately sampled by the recording geometry, the events in the estimated vertical component of the velocity tend to be smeared in the direction of the

Figure 1.23: 2-D isotropic inversion. The image has been divided into 131×26 square cells (10×10 ft^2 each). s2d-iso-hast [NR]

Figure missing !

Figure 1.24: 2-D anisotropic inversion. Each image has been divided into 131 $\times$ 26 square cells (10 $\times$ 10 ft^2 each). Left: V_x. Center: $V_{z\mathrm{NMO}}$. Right: $V_x/V_{z\mathrm{NMO}}$. The spatial resolution of $V_{z\mathrm{NMO}}$ is poor when compared with the spatial resolution of V_x. The ratio $V_x/V_{z\mathrm{NMO}}$ has been separated into four areas that show percentages of anisotropy: white (ratio $>$ 1.25), light gray (1.06 $<$ ratio $\leq$ 1.25), dark gray (0.90 $<$ ratio $\leq$ 1.06), and black (ratio $\leq$ 0.9). The dark gray areas can be considered isotropic. sx2d-hast [NR]

steepest rays, and the spatial resolution in this component is poor when compared with V_{iso} and V_x. In the 1-D case, this lack of information is compensated for by assuming a layered model, which allows us to do more CG-iterations without having problems with the noise. In two dimensions, however, doing more CG-iterations is not possible and therefore the results obtained can be in a stage where V_x is close to convergency but $V_{z\text{NMO}}$ is far from that point. This difference in the speed to convergency of the different components of the velocity may introduce artificial anisotropy.

Because V_x and $V_{z\text{NMO}}$ cannot be estimated at the same resolution (at least using only this type of recording geometry), it is not possible to estimate spatial variations in velocity anisotropy (the ratio $V_x/V_{z\text{NMO}}$ for example) at the same resolution of the variations in velocity. Nevertheless, an image that shows variations in velocity anisotropy can be useful if it accounts only for the large-scale variations that are well resolved by the inversion. Such an image is shown in Figure 1.24. This image is divided into four areas: highly anisotropic, moderately anisotropic, isotropic, and anisotropic with $V_{z\text{NMO}} > V_x$. We can see that most of the model is isotropic whereas the anisotropic areas are associated with high-velocity zones, possibly shales.

Figure 1.25 summarizes how the mean absolute value of the residual (*error*) changes for the different parametrizations used. The error decreases roughly 50 percent from the homogeneous to the 1-D inversion and about 60 percent from the homogeneous to the 2-D inversion, which means that when trying to estimate lateral variations in the medium (smallest singular values), a 10 percent reduction in the mismatch is gained with respect to the estimation of vertical variations only (largest singular values). The residual does not reduce substantially when we compare the 1-D anisotropic inversion (letter D in the plot) with the 2-D isotropic (letter E), with 28 more degrees of freedom, which suggests that anisotropy in the data can be reconciled with either isotropic heterogeneity or anisotropic, less heterogeneous media.

1.5.2 Devine test site

BP's Devine test site is located southwest of San Antonio, Texas. A sketch of the geology at this site is shown in Figure 1.26. This test site has been cited in recent publications to illustrate the application of different techniques. For example, Harris (1988) reports cross-well seismic measurements using a cylindrical piezoelectric bender transducer both as a source and as a receiver. Miller and Chapman (1991) and Onishi and Harris (1991) have concentrated on the problem of estimating velocity anisotropy from cross-well data (tomographically and by head-wave analysis, respectively). Lazaratos et al. (1991) present reflection images also from the cross-well data, and Raikes (1991) has studied the propagation of S-waves from a multicomponent VSP survey.

The cross-well data I used were P-waves with frequencies between 200 Hz and 4000 Hz. They were recorded between two cased boreholes (Wilson 2 and Wilson 4) whose

Figure 1.25: Mean absolute residual for the different parametrizations used. (A): Homogeneous isotropic. (B): Homogeneous anisotropic. (C): 1-D isotropic. (D): 1-D anisotropic. (E): 2-D isotropic. (F): 2-D anisotropic. errors-abs [NR]

separation at the surface is 330 feet. Receivers were separated by 10 feet and sources by 20 feet. Figure 1.26 shows the corresponding sonic logs at each well. Although the variations are mainly one dimensional, it is possible to identify small dips ($\approx$ 1 degree) from the sonic logs at the two wells as well as small lateral variations within thin layers (for example, the top of the Del Rio clay).

A total 1660 traveltimes were picked from a small data set of only 26 gathers. Only those traveltimes corresponding to angles of less than 45 degrees between source and receiver were kept for the inversion.

Figure 1.27 shows the positions of sources and receivers for 10 percent of the data set. The ray coverage is quite irregular, with no horizontal rays sampling large portions of the medium. The horizontal velocities estimated in areas not sampled by

Figure 1.26: Sketch of the geology at the Devine test site with the sonic logs at each well. Although the site is mostly flat layered, small 2-D variations can be seen (modified from Lazaratos et al., 1991). devine-site [NR]

horizontal rays are the horizontal velocities of the best fitting ellipses.

A 1.5-D elliptically anisotropic model was used to fit the data. The starting model (not shown) consisted of 140 horizontal layers five feet thick. The velocity for all layers was 12 000 ft/sec. Layers thinner than one foot were not allowed in the model. The inversion was not constrained to match the vertical velocities or depth of certain layers using information derived from the sonic logs, although the information about dips was already present in the initial model. The dips and the intercepts of the interfaces, as well as the axes of symmetry of the different layers, were allowed to vary during the inversion.

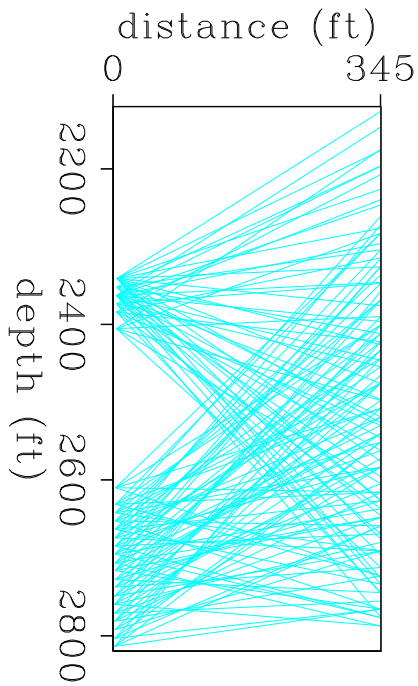

Figure 1.27: Ray coverage for the experiment at the Devine test site for a fraction (10 percent) of the total data set. Notice how irregular the coverage is. devine-rays [NR]

The inversion produced a model with horizontal layers (all dips less than 0.1 degree) and vertical axes of symmetry. Therefore, $V_\perp = V_x$ and $V_{||} = V_{z\text{NMO}}$. Figure 1.28 shows V_x and $V_{z\text{NMO}}$ as well as the average sonic log (V_z) from the two wells, blocked every seven feet. As expected when the anisotropy is caused by fine layering, $V_x > V_z > V_{z\text{NMO}}$ for almost all depths. We also see that $V_{z\text{NMO}}$ is much closer to the sonic log than V_x. In the shale and clay intervals, V_x is more than 30 percent larger than the log velocity The vertical velocity contrast between limestone and shale is greater than 70 percent. Still, the inversion does a good job in estimating $V_{z\text{NMO}}$, which shows the importance of tracing rays appropriately in anisotropic media when doing the inversion. For this model, the average absolute value of the residuals is 0.2 ms (twice the sampling interval). Twelve layers were eliminated during the inversion procedure because their thicknesses fell bellow the one foot threshold.

These results agree with those presented by Miller and Chapman (1991) and Onishi and Harris (1991).

Figure 1.28: 1.5-D inversion at the BP site. An average sonic log (thinner curve) blocked every seven feet is compared with the two estimated velocities. The vertical NMO velocity is closer and better correlated to the log. The amount of anisotropy changes through the model, reaching a peak at the shale and clay intervals. The model is described by 128 layers. devine-log-vel [NR]

Figure 1.28 also shows that the elliptical velocity model explains most of the P-wave anisotropy at this site. The estimated vertical NMO velocity is in general smaller than the log velocity, which is expected if the anisotropy is caused by fine layering. However, the differences between the log velocity and the vertical NMO velocity show that the elliptical model is not fully adequate to describe the possible transverse isotropic nature of this medium. In a few places (the top of the clay, for example) the estimated vertical velocities are larger than the log velocity. This is probably because of lateral variations in the real medium that are not correctly described by the model of heterogeneities.

1.5.3 Biases in the inversion

The main problem considered in the preceding sections was how the limited view of the measurements affects our ability to estimate velocities in different directions. Unfortunately, many other factors besides limited view produce effects that may depend on direction and influence the anisotropy of the results. Among these factors we have:

1. Picking errors. These errors may systematically increase or decrease the velocities, depending on which part of the first arriving wavelet has been picked. Picking before the correct value speeds velocities up, whereas picking later arrivals slows the velocities down. If the picking errors are constant for different vertical offsets, the velocities that result from the inversion can be anisotropic because the errors have more effect on the smaller traveltimes that usually correspond to rays that travel horizontally. Picking errors may explain why in Figure 1.21 $V_{z\mathrm{NMO}}$ is systematically one or two percent faster than the sonic log.

2. Head waves picked as body waves. Although this bias may be considered a picking error, it primarily affects traveltimes from small vertical offsets (i.e., ray paths close to the horizontal) in low-velocity layers. Traveltimes from head waves picked as body waves affect S_x more than $S_{z\mathrm{NMO}}$ because $S_{z\mathrm{NMO}}$ is less sensitive to rays that travel at small angles. Therefore, when head waves are inverted like body waves, the estimated horizontal velocity may turn out to be faster than the actual one.

3. Well deviation. Often, wells deviate in three dimensions but the results are rarely presented in three dimensions. Instead, the 3-D deviations are usually projected onto a 2-D plane where conventional 2-D algorithms can be applied. If the well deviation is not strong, and if the 3-D variations in the real medium are moderate, the 2-D solution is a good approximation but otherwise it may not be. I didn't consider the well deviation when first testing the algorithm with field data. When comparing the velocities that were estimated without considering well deviation with those estimated by considering it (Figure 1.21), I obtained higher velocities where the wells were actually closer and lower velocities where

the wells were actually farther apart. S_x was more sensitive to well deviation than $S_{z\text{NMO}}$.

All these factors, when not considered correctly, may produce artificially anisotropic results, especially when complex models are used to describe both anisotropy and heterogeneity.

1.6 Conclusions

This chapter has presented the basic theory and examples of an algorithm that does anisotropic traveltime tomography. The algorithm generalizes the well-known techniques of tomographic traveltime inversion in isotropic media by using models discretized into a set of homogeneous elliptically anisotropic cells. Each cell is characterized by two slownesses, and the inclination of the axis of symmetry.

Cross-well geometries usually don't adequately sample the vertical component of the medium's velocity. The opposite happens with the horizontal component of the velocity. Therefore, it is easier to estimate V_x than V_z when using cross-well geometries alone.

In one dimension, both components of the slowness can be estimated accurately if the range of ray angles that is wide enough. Otherwise the problem becomes ill-conditioned. In two dimensions, however, the vertical component of the velocity has poor resolution when compared to the horizontal component. Therefore, the spatial resolution in velocity anisotropy is also poor. In general, it is difficult to separate small variations in velocity anisotropy from reconstruction artifacts.

I have found that 1.5-D models, which consist of dipping elliptically anisotropic layers, are a good compromise between the simplicity and restricted applicability of 1-D models and the complexity and generality of full 2-D models. I use 1.5-D models to illustrate the estimation of velocity anisotropy in a medium with strong anisotropy, strong velocity contrasts, and variable inclination of the axis of symmetry.

When the measurements have limited view, and iterative techniques such as conjugate gradients are used to solve the linearized problem, early termination of the iterations may produce artificial anisotropy. This problem is more severe in 2-D than in 1-D estimation of velocity anisotropy.

Since the inclination of the axis of symmetry is also a variable in the inversion procedure, certain types of azimuthally anisotropic media can be approximated, in particular those formed by dipping, transversely isotropic layers.

The estimated elliptical velocities can be transformed into elastic constants that describe a general TI medium, if compressional and shear wave traveltimes are available. The next chapter addresses this topic. If any of the wave types is not available, the partial solutions obtained are still useful since they can be interpreted in terms of medium properties such a lithology or fine layering, as the field data examples in this chapter show.